Structural and electronic properties of two-dimensional freestanding BaTiO₃/SrTiO₃ heterostructures

Fanhao Jia,[*] Shaowen Xu [©],[*] Guodong Zhao, Chao Liu, and Wei Ren[†]

Physics Department, Shanghai Key Laboratory of High Temperature Superconductors, State Key Laboratory of Advanced Special Steel, International Centre of Quantum and Molecular Structures, Shanghai University, Shanghai 200444, China

The successful preparation of the freestanding perovskite materials down to the monolayer limit [Ji *et al.*, Nature (London) **570**, 87 (2019)] provided the opportunity to make the two-dimensional (2D) oxide and heterostructure, which could be significantly distinctive from the conventional oxide superlattices and other 2D van der Waals heterostructures. By stacking one unit-cell BaTiO₃ (BTO) and one unit-cell SrTiO₃ (STO) on top of each other, we constructed two isolated bilayers of the 2D heterostructure systems. From our density functional theory simulation, their ground states exhibit an in-plane ferroelectricity in both BTO layer and STO layer, while the antiferrodistortive mode of the STO layer is totally suppressed. These two systems show band gaps in the range of 2–2.5 eV (by using HSE06), which are smaller than their monolayer and bulk phases. The layer arrangement strongly influences their electronic properties. We reveal that they adopt the type-II electronic band alignment. The tensile biaxial strain can strongly promote the ferroelectricity and increase the band gaps of these systems. Our results will contribute to the further understanding of layered materials based on the transition metal oxide perovskites and developing relevant experimental devices.

I. INTRODUCTION

The two-dimensional (2D) freestanding transition-metal oxide perovskite greatly expands the range of available 2D material systems and offers tremendous opportunities for designing new 2D multifunctional materials [1,2]. The experimental technique of growing high-quality oxide crystals layer-by-layer guarantees the convenience of combining these perovskites of different functions into heterostructures. One of the potentially inspiring combinations is with the ferroelectric (FE) and paraelectric (PE). The fascination comes from the fact that the strongly tunable balance between two major instabilities, namely the FE modes (polar displacements) and the antiferrodistortive (AFD) modes (rotation or tilting of the oxygen octahedron) [3–5], can enhance and reach desired properties in systems such as their mixture [6] or superlattice [7–10].

Much effort has been made to study the ferroelectric properties of FE/PE BaTiO₃/SrTiO₃ (BTO/STO) superlattices theoretically and experimentally [11,12]. These two oxide materials show a lattice mismatch of 2.4% in their cubic phases [13]. Under the short stacking periodicity condition, the paraelectric STO layer is induced to exhibit both in-plane ([110]) and out-of-plane ([001]) polarization, while the BTO layer only maintained the out-of-plane ([001]) polarization [14,15]. When the number of BTO layers is equal to that of the

STO layers, a reduced polarization arising from the hardening and modification of local soft modes at the interface was found [16]. However, this remanent polarization could be enhanced by controling the thickness ratio of STO and BTO [15,17] and tensile strain [18], which could be two times larger than that in the single-phase BTO film and even larger than the value of the BTO bulk [19]. To the best of our knowledge, freestanding BTO/STO heterostructures have not been discussed down to the ultrathin 2D limit in the literature. In contrast with the conventional van der Waals heterostructures [20], the layers in oxide heterostructures are chemically stacked by the ionic bonds. As a result, there is no complex issue of relative stacking [21] and twisting angle [22] problems. On the other hand, due to the intrinsic out-of-plane symmetry breaking of the ABO_3 monolayer, the layer arrangement and strong interfacial coupling are expected to affect the functionality. Therefore, it is very important to clarify the microscopic origin and assess how these characteristics benefit the quantum electronics device design.

Here, to determine theoretically the ground state properties, we performed first-principles simulations on two types of heterostructures, namely BTO/STO and STO/BTO, according to the layer stacking order arrangement. First, the polarization behavior is carefully investigated, and we emphasize that the in-plane FE is strongly related with layer interactions. Then, we focus on the layer stacking dependence of the electronic properties. We further show how the biaxial strain modifies its structural and electronic characteristics, which will enhance the understanding of strain effects on polarization and electronic properties.

---

[*]These authors contributed equally to this work.
[†]renwei@shu.edu.cn

II. COMPUTATIONAL DETAILS

We performed the density functional theory (DFT) calculations as implemented in the Vienna *ab initio* simulation package (VASP) [23] using the projector-augmented wave approach [24,25]. We take the $4s$, $4p$, $5s$ as the valence electrons for Sr, $3s$, $3p$, $3d$, $4s$ for Ba, $3s$, $3p$, $3d$, $4s$ for Ti, and $2s$, $2p$ for O. The generalized gradient approximation (GGA) in the form proposed by Perdew, Burke, and Ernzerhof (PBE) [26], and the revised version for solids (PBEsol) [27] were adopted for the exchange correlation energy. The heterostructure geometry is constructed from the prototype paraelectric structure of STO (space group I4/mcm), where we replace one Sr-O layer by a Ba-O layer, and a vacuum space of more than 20 Å is added for achieving the 2D slab. Then, we identified instabilities from the inspection of the phonon dispersion curves (see Fig. S1 [28]), accordingly lowered the crystal symmetry, and performed structural relaxations. Furthermore, we also performed two molecular dynamics simulations based on $2 \times 2 \times 1$ supercell (see Fig. S2). We extracted the structure with the lowest energy and re-relaxed it, which showed very consistent structure and energy with that from the phonon method. The energy cutoff was chosen to be 600 eV for all calculations. A $6 \times 6 \times 1$ Γ centered Monkhorst-Pack k-points grid in the Brillouin zone was used here. The convergence criterion of energy was set to at least smaller than 10^{-6} eV and atomic positions were fully relaxed until the maximum force on each atom was less than 10^{-3} eV/Å. To address the well-known problem of underestimating the band gap, the screened hybrid functional proposed by Heyd, Scuseria, and Ernzerhof (HSE06) [29] was applied to investigate electronic band properties. The mixing of Hartree-Fock to GGA ratio was 0.25:0.75 and a screening parameter of 0.2 Å^{-1} was adopted. The phonon dispersion spectra were calculated based on a $2 \times 2 \times 1$ supercell using the density-functional perturbation theory (DFPT) method as implemented in the PHONOPY package [30,31]. In this method, the electron-density linear response of a system can be calculated by taking the atomic displacement as a perturbation potential, which determines the matrix of its interatomic force constants [32]. This theory of lattice dynamics calculation is also valid in 2D systems, and can achieve phonon dispersions well comparable with experiments in systems such as graphene and others [33,34]. It is worth mentioning that the acoustic out-of-plane mode of 2D materials has a quadratic dispersion, as explained by Lifshitz [35]. The layer resolved in-plane polarizations were computed by multiplying the atomic off-shift vectors from their high symmetry positions with the Born effective charges tensors, which were calculated by DFPT. The calculated value of 2D polarization strongly depends on the thickness of slab we choose. Here, we applied two additional 1 Å space on two sides of the heterostructures for the calculation of volume Ω. The Born effective tensor is defined as: $Z_{i,j}^* = \frac{\Omega}{e} \frac{\partial P_i}{\partial u_j}$ where e is the charge of one electron, P is polarization, and u is the atom's displacement from its high-symmetry nonpolar position. The total out-of-plane polarizations are calculated by the integral of charge density. The biaxial strain was defined as $\varepsilon(\%) = \frac{a - a_0}{a_0}$, where a and a_0 are the strained and equilibrium lattice constants. We varied the in-plane strain from -3%

TABLE I. The layer resolved in-plane polarizations from Born effective charges and atomic displacements, as well as the total out-of-plane polarizations from the integral of charge density.

	BTO/STO		STO/BTO	
	$P_x(\mu C/cm^2)$	$P_y(\mu C/cm^2)$	$P_x(\mu C/cm^2)$	$P_y(\mu C/cm^2)$
BaO	−0.14	0.00	−0.14	0.00
1-TiO$_2$	−0.51	0.00	−0.09	0.00
SrO	−0.72	0.00	−0.53	0.00
2-TiO$_2$	−6.76	0.00	−11.01	0.00
$P_z(\mu C/cm^2)$	18.51		9.19	

to 3% with a step length of 0.01 Å, and further relaxed the structures with constrains.

III. RESULTS AND DISCUSSION

A. The ground structure

We display the side view of the unit-cell BTO/STO or STO/BTO heterostructure in Fig. 1(a), which contains 20 atoms in total. It is easy to find that these systems naturally show an out-of-plane symmetry breaking. Here, we define the BTO/STO case as that the top layer is the Ba-O layer and the bottom layer is the Ti-O layer, whereas the STO/BTO case is where the top layer is the Sr-O layer and the bottom layer is the Ti-O layer. These heterostructures contain 1.5-layers oxygen octahedra, which are illustrated by layer 1 and layer 2 in Figs. 1(c) and 1(d). The BTO/STO case has a lattice constant of $a = 5.575$ Å and $b = 5.567$ Å, while the STO/BTO has $a = 5.590$ Å and $b = 5.583$ Å . Both cases maintain a mirror symmetry plane that is perpendicular to the b axis, so there is no polarization along the b axis. On the other hand, due to the Ti-O bond length relation of $m_2 > m_1 > n_1 > n_2$, there are in-plane polarizations along the a axis existing in both the STO layer and BTO layer.

We list the layer resolved the in-plane polarizations in Table I (please also see the detailed displacements of Ti-O layer, Ba-O layer and Sr-O layer in Table SI). The STO/BTO shows a larger P_x than the BTO/STO. It is easy to find that the in-plane polarizations are mainly from the layer 2, especially from the 2-TiO$_2$ layer. The A-O layers present relatively small contributions to the total polarization, even though they also show considerable displacements due to the interfacial coupling. We also notice that the Δ_{Sr-O} is more sensitive to the layer arrangement than the Δ_{Ba-O}.

The total energies as function of the amplitudes of the in-plane and out-of-plane distortions are displayed in the Fig. 1(b), where an interpolation parameter λ is introduced to represent the distortions with respect to the high-symmetry structure. We note that the in-plane displacements result in a double-well-like potential with a small energy barrier between two local minima, which means that this in-plane polarization is switchable, i.e., ferroelectric. The well depths ΔE of BTO/STO and STO/BTO are much smaller than that of the bulk BTO ($\sim$10 meV/atom [13]), suggesting that their ferroelectricity is relatively weak. On the other hand, the
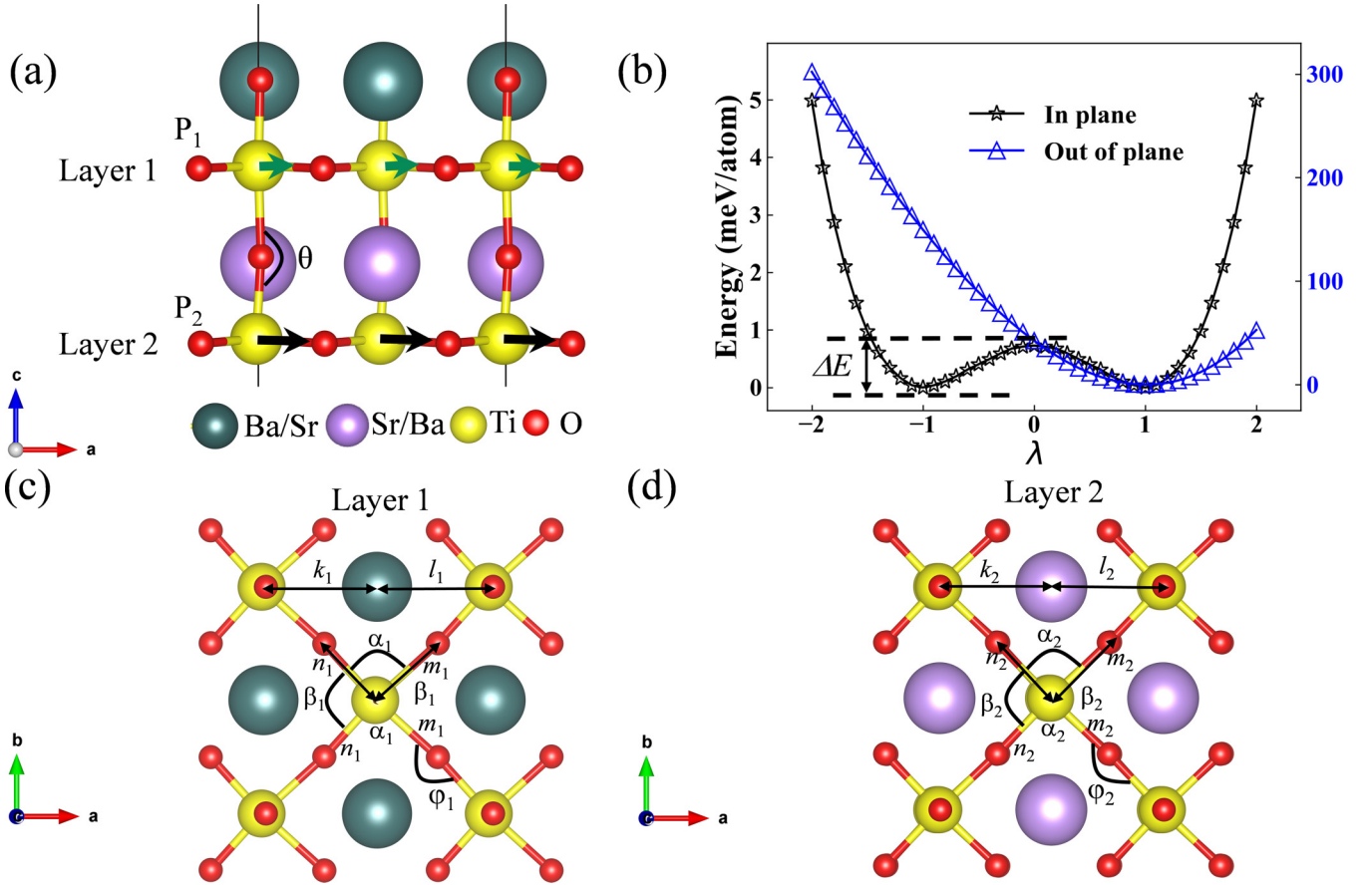
FIG. 1. (a) Schematic diagram of the structural characteristics. The side view of BTO/STO or STO/BTO heterostructures, where the arrows represent the in-plane polarization along the *a*-axis direction. The length of the arrow represents the magnitude of the displacement. An out-of-plane angle θ of Ti-O-Ti between two layers is defined. (b) The total energies of BTO/STO as function of the amplitudes of the in-plane and out-of-plane distortions, where the ΔE (meV/atom) is the double-well depth. The $\lambda = \pm 1, 0$ and in between represent the ground structure, high-symmetric structure, and the extrapolated structure, respectively. (c), (d) The in-plane structural characteristics of two layers, where *i* is the layer index, φ is the angle between two adjacent octahedra, α and β are the in-plane O-Ti-O bond angles, *n* and *m* are the Ti-O bond lengths, and their difference $\Delta_i = m_i - n_i$ represents the displacement of each Ti-O layer.

out-of-plane displacements are not switchable as there is only one energy minimum. This is due to that the out-of-plane displacements have particular preferences in the choice of directions, for example, the Ti^{4+} of layer 2 always shows the trend to approach to the O^{2-} above it.

We note that an in-plane polarization is also present in bilayer BTO systems. From the one-electron perspective, the in-plane distortions are partially derived by the hybridization between the low-lying empty Ti^{4+} 3*d* states and the O^{2-} 2*p* states (i.e., second-order Jahn-Teller effect [36]), which is believed to be the mechanism of ferroelectricity in their bulk systems [37]. On the other hand, the bilayer STO system is consistent with its bulk as well, which has no in-plane polarization. Hence, the in-plane ferroelectricity of the STO layer in the heterostructure is mostly from the interaction with the BTO layer, or the tensile strain due to the mismatch of two cation radii. In addition, we should notice that the Δ_2 is always much larger than Δ_1, which indicates that the dominant factor for the intensity of the layer-resolved ferroelectricity is the different boundary conditions of two Ti-O layers, besides the chemical difference of the *A*-site cations.

The detailed interatomic distances of our systems are listed in Table II, where we find that the Ti^{4+} and *A*-site ions (Ba^{2+} or Sr^{2+}) show quite different tetragonality, which also depends on the layer arrangement. The electrostatic potential energy difference $\Delta\varphi$ between the two sides of the heterostructure is also listed in Table II, which implies the existing of an intrinsic built-in electric field along the *c* direction. By comparing the bilayer systems and our heterostructures, we find the $\Delta\varphi$ is almost dominated by the *A*-site ion of the layer 2.

The oxygen octahedra rotation or tilting, namely the AFD mode, is another important ordering of the structural properties, which is known to compete with FE [38,39] in most cases of perovskites [9]. If we still treat the 1.5-layer oxygen octahedron as "two-layer octahedral," we find both heterostructures to be $a^0b^0c^0$ by the Glazer notation [40]. In our systems, the AFD of STO layer is almost fully suppressed, which is also confirmed by our phonon calculations. This is quite different with the bilayer STO system, which shows apparent rotation of the octahedron. Therefore, we think the competitive relationship between the AFD and FE is in our system should be one of the reasons for the weak in-plane

TABLE II. The PBEsol optimized lattice parameters: a_{Ti}(Å) is the in-plane distance between two nearest Ti^{4+}, c_{Ti}(Å) is the distance between two Ti^{4+} in different layers, $(c/a)_{Ti} = c_{Ti}/a_{Ti}$, c_A(Å) is the distance between two A-site ions (Ba^{2+} or Sr^{2+}) of each layer, $(c/a)_A = c_A/a_A$ where $a_A = a_{Ti}$, a_b(Å) and $(c/a)_b$ are the lattice constants of their bulk tetragonal phases. The electrostatic potential energy differences $\Delta\varphi$ (eV) between the two sides are presented.

System	a_{Ti}	c_{Ti}	$(c/a)_{Ti}$	c_A	$(c/a)_A$	a_b	$(c/a)_b$	$\Delta\varphi$ (eV)
Bilayer BTO	3.939	3.981	1.011	4.049	1.028	3.966	1.024	5.28
Bilayer STO	3.850	3.893	1.011	3.890	1.010	3.886	1.006	5.05
BTO/STO	3.890	3.859	0.992	4.061	1.044			5.04
STO/BTO	3.901	4.029	1.032	3.885	0.996			5.34

polarization. Another reason may relate to the more dominant out-of-plane polarization, which results in a built-in electric field intrinsically reducing the in-plane polarization.

B. The electronic properties

We illustrate the HSE06 band structures of two heterostructures in Figs. 2(a) and 2(b). First, they are direct bandgap semiconductors with valence band maximum (VBM) and conduction band minimum (CBM) both located at the Γ point. They display similar VBM but different CBM, so that the STO/BTO shows a smaller effective mass in the CBM as well as a 0.5 eV smaller band gap than the BTO/STO. We summarize the band gaps of their heterostructures, monolayers, bilayers, superlattice, and bulks systems in Table III. We found that the band gap of the heterostructure is also mainly determined by A-site ion of layer 2. The related monolayer, superlattice, and bulk systems show similar band gaps, which are about $0.6\,eV \sim 1.3\,eV$ larger than the bilayer and heterostructures systems. Hence, the calculated band gaps are found to be dependent on the layer stacking arrangement, and also on the number of component layers.

The projected density of states (PDOS) of two heterostructures are provided in the Fig. 3. Their VBM is mainly derived by the Op_x and Op_y with a little hybridization of Sr in the BTO/STO and Ba in the STO/BTO case, while their CBM is mainly derived by the empty states of Ti atoms with a little hybridization of Ba in the BTO/STO and Sr

in the STO/BTO case. Because of the VBM and CBM are derived from different compounds, these heterostructures are categorized to have type-II band alignment. Under such a circumstance, the generated electron-hole pairs are naturally separated in space, which may promote the efficiency of the possible photocatalytic and photovoltaic devices [43,44].

C. The strain engineering

The ferroelectricity is sensitive to the epitaxial mismatch strain, same as the lattice distortions, dielectric constant, and phase transition temperature T_C [45]. Over the past decades, a vast number of perovskites have been successfully utilized as substrates in the synthesis of artificial thin films. With such a broad range of lattice constants as shown in Fig. 4, the mismatch strain can be experimentally adjusted within $[-3\%, 3\%]$ for many perovskites. In Figs. 4(a) and 4(b), we show the strain effect on the Δ_i, α_i, β_i, and φ_i defined in Fig. 1 and Table SI. One may notice that all of such angles in our heterostructures are not equal to 90° or 180°. However, these angles only represent the deformation of the oxygen octahedron that arises because of the FE distortions. Therefore, what we want to emphasize is that there is only the deformation of oxygen octahedron but no tilting of octahedron in our heterostructures. The difference between the deformation and tilting of the octahedron is illustrated in Fig. S3. The first thing we find is that the Δ_1 is more easily suppressed to zero than the Δ_2 under compressive strain, and Δ_2 is always much
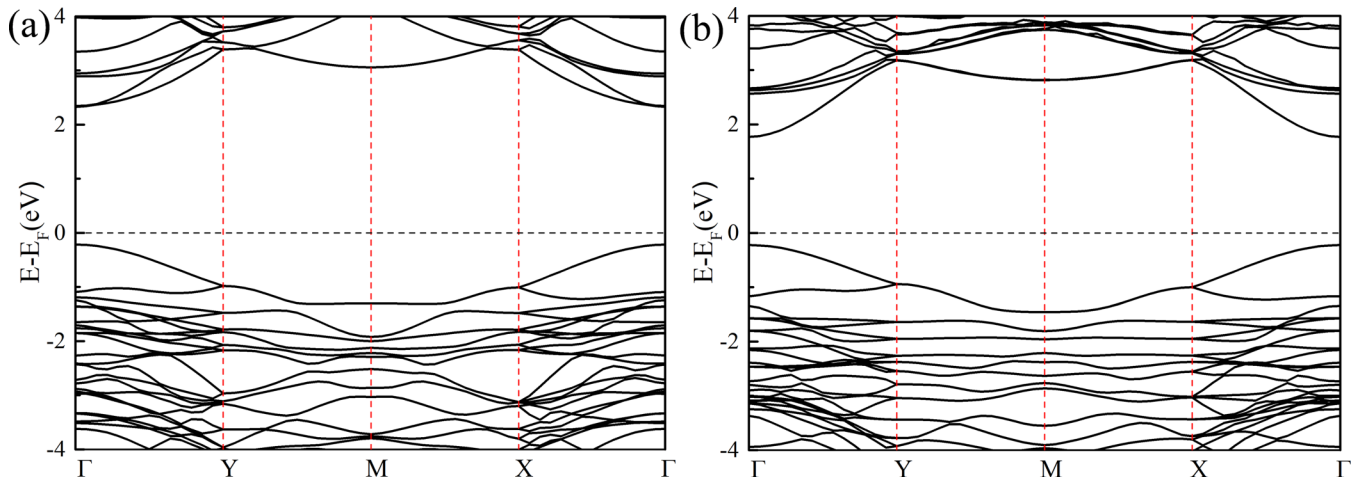

FIG. 2. The electronic band structures of (a) BTO/STO and (b) STO/BTO heterostructures by using the HSE06 functional.

TABLE III. The calculated band gaps (eV) of BTO/STO and STO/BTO heterostructures, monolayer STO and BTO, bilayer STO and BTO, $(BTO)_1/(STO)_1$ superlattice, bulk tetragonal STO and BTO.

System	Energy Gap(eV)		
	PBE	PBEsol	HSE
BTO/STO	1.05	0.93	2.54
STO/BTO	0.52	0.48	1.99
Monolayer STO [41]	1.77	/	3.13
Monolayer STO	1.72	1.77	3.34
Monolayer BTO	1.81	1.67	3.03
Bilayer STO	0.81	0.82	2.40
Bilayer BTO	0.98	0.69	2.24
$(BTO)_1/(STO)_1$	1.75	1.77	3.12
Bulk STO [42]	1.79	1.93	3.11
Bulk BTO [42]	1.76	1.76	3.02

larger than the Δ_1. We also combined our DFT results with the AMPLIMODES [46] analysis to explore the distortions as shown in Fig. 4(c). As we know, the total displacements have a positive correlation with the in-plane polarization. Therefore, the tensile strain significantly enhances the spontaneous in-plane polarization, vice versa. As mentioned in the bottom-up, layer-by-layer growth technique in the latest literature [1], the

freestanding oxide perovskites layer can be transferred onto any desired substrate, such as crystalline silicon wafers and holey carbon films. We have added the available substrates indicated in Fig. 4(c) to represent the strain of some examples, and also physical property changes versus lattice mismatch strain. As shown in Fig. 4(d), the BTO/STO transforms to a PE phase under a 0.5% compressive strain, while the STO/BTO case becomes a PE phase under a 1.3% compressive strain. The double well depth ΔE is strongly related with the T_C, which can be increased by more than one order of magnitude by a 3% tensile strain as shown in Fig. 4(d). We also present the energy gap of the two heterostructures at various misfit strains in Fig. 4(d). Overall, the band gap is increased by the tensile strain, with a similar trend of the FE distortions. Quantitatively a 3% tensile strain can increase the band gap of STO/BTO from ~0.5 eV to 1 eV, and from 0.9 eV to 1.5 eV for the BTO/STO case. We also observed that the energy gap of BTO/STO is wider than the STO/BTO system in all the applied strain range, which is derived from the Ti $3d_{yz}$ gradually moving away from the Fermi level. All in all, we demonstrate that the biaxial strain gives a remarkable control on the properties of the 2D freestanding heterostructures.

IV. CONCLUSION

In summary, we calculated the structural and electronic properties of the freestanding 2D BTO/STO and STO/BTO
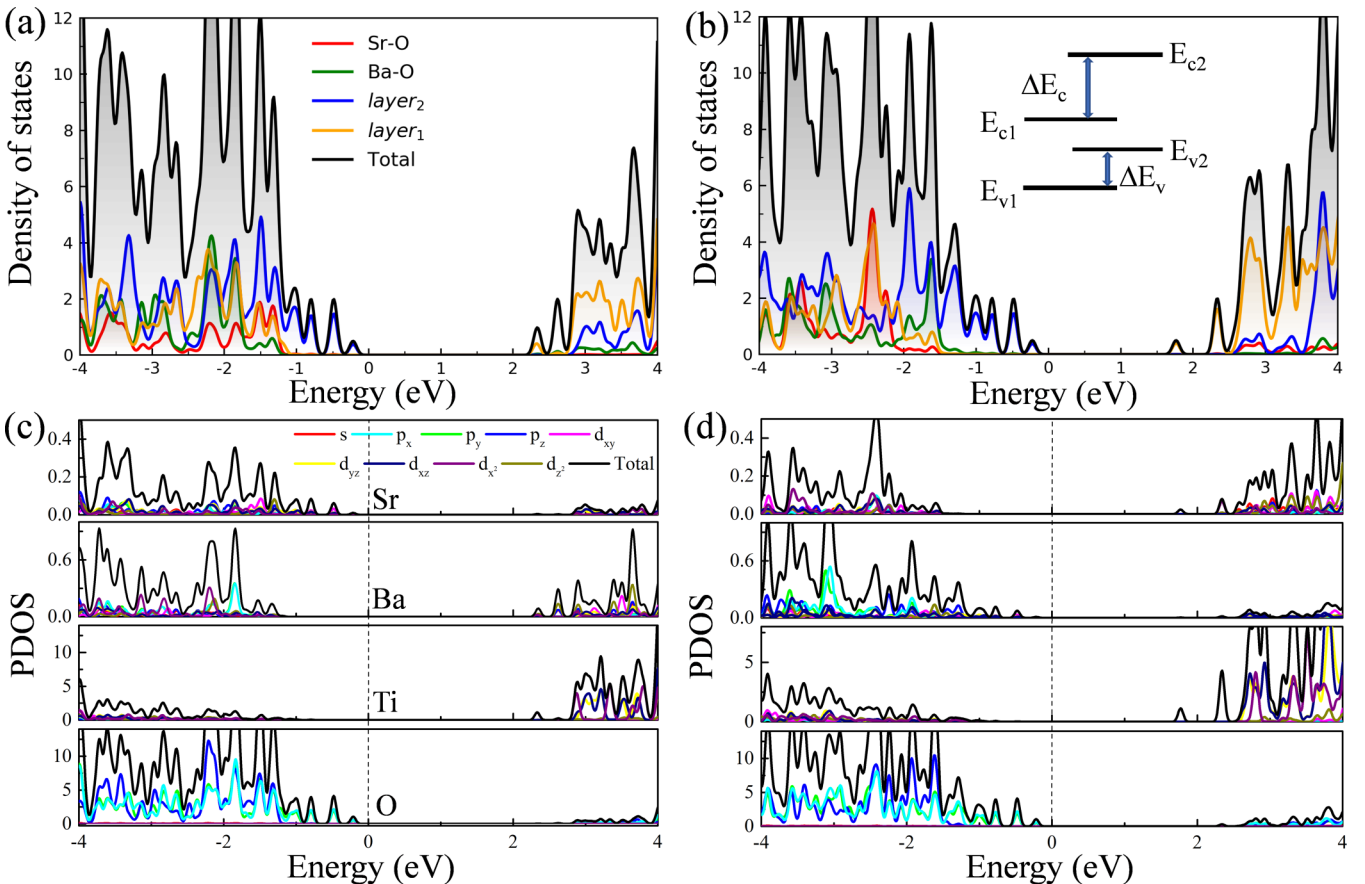

FIG. 3. The total and projected density of states (PDOS) calculated by HSE06, onto the Sr-O layer, Ba-O layer, layer 1, and layer 2 for (a) BTO/STO and (b) STO/BTO heterostructures. The PDOS of each element and each orbital is shown in (c) BTO/STO (d) STO/BTO.
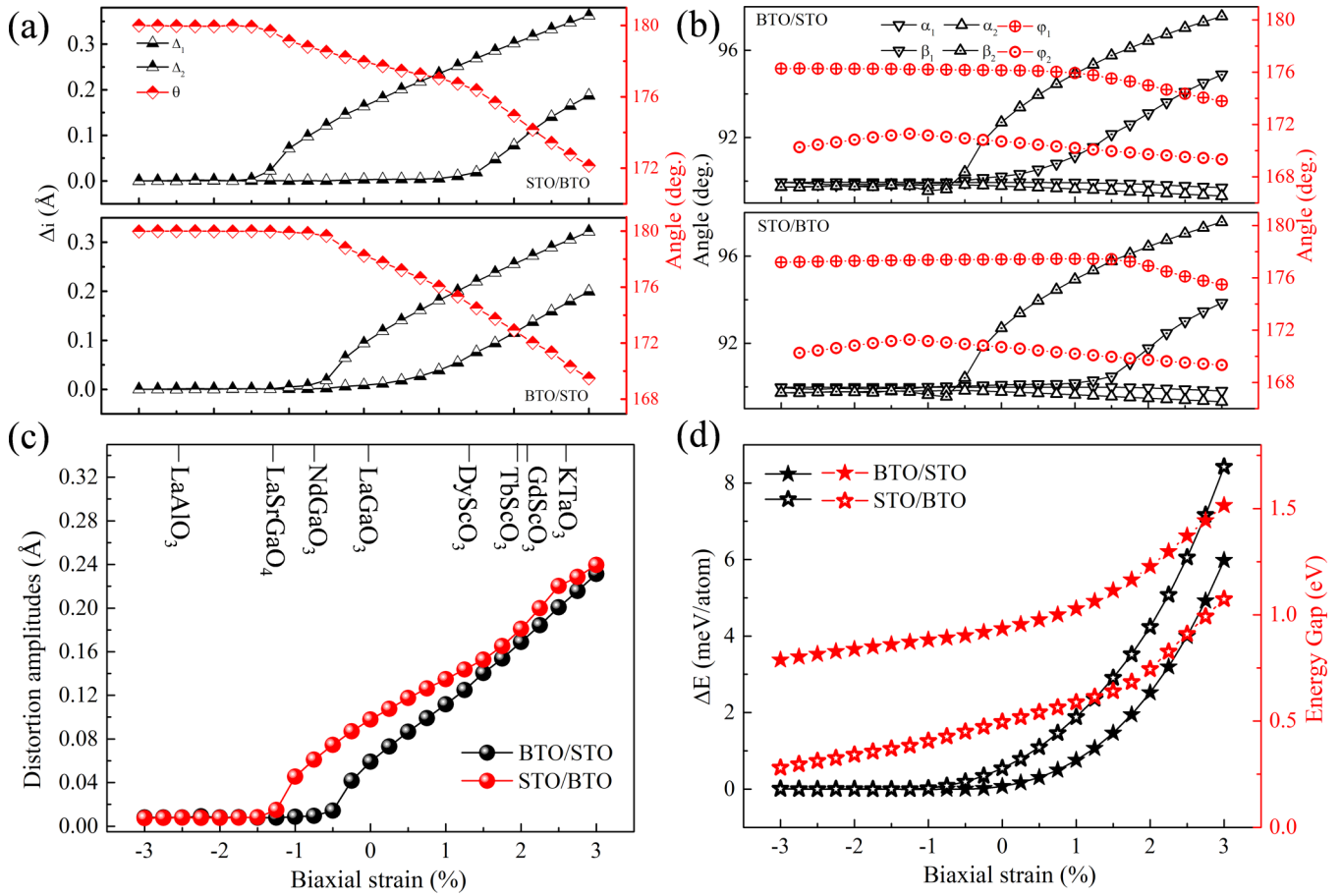
FIG. 4. (a) The Ti-O bond difference Δ_i and the Ti-O-Ti angle in two heterostructures as functions of the biaxial strain. (b) The in-plane angle α_i, β_i and out-of-plane φ_i as functions of biaxial strain. (c) The amplitude of the normalized total displacement distortion as functions of biaxial strain. (d) The double well depth of ΔE and band gaps calculated by using PBEsol as functions of biaxial strain.

heterostructures. These two systems present in-plane ferroelectric polarization, while the AFD is suppressed by the interface interaction. They show type-II band alignment with direct band gaps, for the two-layer arrangements considered in this work. Furthermore, we reveal that the band gap and the ferroelectricity properties are significantly dependent on the strain. Compared to conventional 2D materials, which usually involve s and p electrons, the transition-metal oxide perovskites with d electrons have richer degrees of freedom and more exotic phases. Our work presents some interesting features of the ultrathin freestanding oxide perovskite heterostructures that may be useful for further investigating fundamental interfacial physics and strongly correlated properties when approaching the 2D limit.

[1] D. Ji, S. Cai, T. R. Paudel, H. Sun, C. Zhang, L. Han, Y. Wei, Y. Zang, M. Gu, Y. Zhang *et al.*, Nature (London) **570**, 87 (2019).

[2] G. Dong, S. Li, M. Yao, Z. Zhou, Y.-Q. Zhang, X. Han, Z. Luo, J. Yao, B. Peng, Z. Hu *et al.*, Science **366**, 475 (2019).

[3] K. Miura and M. Tanaka, Jpn. J. Appl. Phys. **37**, 6451 (1998).

[4] R. F. Berger, C. J. Fennie, and J. B. Neaton, Phys. Rev. Lett. **107**, 146804 (2011).

[5] M. Li, J. Li, L.-Q. Chen, B.-L. Gu, and W. Duan, Phys. Rev. B **92**, 115435 (2015).

[6] Z. Gu, S. Pandya, A. Samanta, S. Liu, G. Xiao, C. J. Meyers, A. R. Damodaran, H. Barak, A. Dasgupta, S. Saremi *et al.*, Nature (London) **560**, 622 (2018).

[7] D. G. Schlom, L.-Q. Chen, C.-B. Eom, K. M. Rabe, S. K. Streiffer, and J.-M. Triscone, Annu. Rev. Mater. Res. **37**, 589 (2007).

[8] J. Bonini, J. W. Bennett, P. Chandra, and K. M. Rabe, Phys. Rev. B **99**, 104107 (2019).

[9] P. Aguado-Puente, P. Garcia-Fernandez, and J. Junquera, Phys. Rev. Lett. **107**, 217601 (2011).

[10] E. Bousquet, M. Dawber, N. Stucki, C. Lichtensteiger, P. Hermet, S. Gariglio, J.-M. Triscone, and P. Ghosez, Nature (London) **452**, 732 (2008).

[11] A. I. Lebedev, J. Adv. Dielectrics **2**, 1250003 (2012).

[12] S. Rios, A. Ruediger, A. Jiang, J. Scott, H. Lu, and Z. Chen, J. Phys. Condens. Matter **15**, L305 (2003).

[13] F. Jia, G. Kresse, C. Franchini, P. Liu, J. Wang, A. Stroppa, and W. Ren, Phys. Rev. Mater. **3**, 103801 (2019).

[14] K. Johnston, X. Huang, J. B. Neaton, and K. M. Rabe, Phys. Rev. B **71**, 100103(R) (2005).

[15] T. Shimuta, O. Nakagawara, T. Makino, S. Arai, H. Tabata, and T. Kawai, J. Appl. Phys. **91**, 2290 (2002).

[16] J. H. Lee, J. Yu, and U. Waghmare, J. Appl. Phys. **105**, 016104 (2009).

[17] H. N. Lee, H. M. Christen, M. F. Chisholm, C. M. Rouleau, and D. H. Lowndes, Nature (London) **433**, 395 (2005).

[18] L. Kim, J. Kim, D. Jung, J. Lee, and U. V. Waghmare, Appl. Phys. Lett. **87**, 052903 (2005).

[19] J. Neaton and K. Rabe, Appl. Phys. Lett. **82**, 1586 (2003).

[20] G. W. Mudd, S. A. Svatek, L. Hague, O. Makarovsky, Z. R. Kudrynskyi, C. J. Mellor, P. H. Beton, L. Eaves, K. S. Novoselov, and Z. D. Kovalyuk, Adv. Mater. **27**, 3760 (2015).

[21] Y. Wu, W. Xia, W. Gao, F. Jia, P. Zhang, and W. Ren, 2D Mater. **6**, 015018 (2018).

[22] A. Mishchenko, J. Tu, Y. Cao, R. Gorbachev, J. Wallbank, M. Greenaway, V. Morozov, S. Morozov, M. Zhu, and S. Wong, Nat. Nanotechnol. **9**, 808 (2014).

[23] G. Kresse and J. Furthmüller, Phys. Rev. B **54**, 11169 (1996).

[24] C. J. Först, C. R. Ashman, K. Schwarz, and P. E. Blöchl, Nature (London) **427**, 53 (2004).

[25] G. Kresse and D. Joubert, Phys. Rev. B **59**, 1758 (1999).

[26] J. P. Perdew, K. Burke, and M. Ernzerhof, Phys. Rev. Lett. **77**, 3865 (1996).

[27] G. I. Csonka, J. P. Perdew, A. Ruzsinszky, P. H. T. Philipsen, S. Lebègue, J. Paier, O. A. Vydrov, and J. G. Ángyán, Phys. Rev. B **79**, 155107 (2009).

[28] See Supplemental Material at http://link.aps.org/supplemental/10.1103/PhysRevB.101.144106 for the phonon spectrum, MD simulations, the schematic diagram of the tilting and deformation of oxygen octahedral and further structural parameter characteristics.

[29] J. Heyd, G. E. Scuseria, and M. Ernzerhof, J. Chem. Phys. **118**, 8207 (2003).

[30] A. Togo, F. Oba, and I. Tanaka, Phys. Rev. B **78**, 134106 (2008).

[31] A. Togo and I. Tanaka, Scr. Mater. **108**, 1 (2015).

[32] S. Baroni, S. deGironcoli, and P. Dal Corso, Rev. Mod. Phys. **73**, 515 (2001).

[33] F. Liu, P. Ming, and J. Li, Phys. Rev. B **76**, 064120 (2007).

[34] J.-A. Yan, W. Y. Ruan, and M. Y. Chou, Phys. Rev. B **77**, 125401 (2008).

[35] I. Lifshitz, Zh. Eksp. Teor. Fiz **22**, 475 (1952).

[36] J. M. Rondinelli, A. S. Eidelson, and N. A. Spaldin, Phys. Rev. B **79**, 205119 (2009).

[37] R. E. Cohen, Nature (London) **358**, 136 (1992).

[38] I. A. Kornev, L. Bellaiche, P.-E. Janolin, B. Dkhil, and E. Suard, Phys. Rev. Lett. **97**, 157601 (2006).

[39] U. Aschauer and N. A. Spaldin, J. Phys. Condens. Matter **26**, 122203 (2014).

[40] A. Glazer, Acta Crystallogr. B **28**, 3384 (1972).

[41] X.-B. Xiao and B.-G. Liu, arXiv:1907.00898 (2019).

[42] R. Wahl, D. Vogtenhuber, and G. Kresse, Phys. Rev. B **78**, 104116 (2008).

[43] J. Zhang, M. Deng, Y. Yan, T. Xiao, W. Ren, and P. Zhang, Phys. Rev. Appl. **11**, 044052 (2019).

[44] R. K. Biroju, D. Das, R. Sharma, S. Pal, L. P. Mawlong, K. Bhorkar, P. Giri, A. K. Singh, and T. N. Narayanan, ACS Energy Lett. **2**, 1355 (2017).

[45] J. Haeni, P. Irvin, W. Chang, R. Uecker, P. Reiche, Y. Li, S. Choudhury, W. Tian, M. Hawley, B. Craigo et al., Nature (London) **430**, 758 (2004).

[46] D. Orobengoa, C. Capillas, M. I. Aroyo, and J. M. Perez-Mato, J. Appl. Crystallogr. **42**, 820 (2009).